Tectonophysics 578 (2012) 76–86

Contents lists available at SciVerse ScienceDirect

Tectonophysics

journal homepage: www.elsevier.com/locate/tecto

Fault zone Q values derived from Taiwan Chelungpu Fault borehole seismometers (TCDPBHS)

Yu-Ju Wang *, Yen-Yu Lin, Meng-Chieh Lee, Kuo-Fong Ma

Institute of Geophysics, National Central University, Chungli, Taiwan

ARTICLE INFO

Article history:
Received 30 November 2010
Received in revised form 13 October 2011
Accepted 19 December 2011
Available online 29 December 2011

Keywords:
Chelungpu Fault
Qp
Qs
Seismic attenuation
Taiwan Chelungpu Fault Drilling Project
Fault-zone attenuation

ABSTRACT

The attenuation factor, *Q*, at a fault zone is an important parameter for understanding the physical properties. In this study, we investigated the *Q* value of the Chelungpu Fault, the main rupture of the Mw 7.6 Chi-Chi earthquake, using the 7-level TCDP borehole seismometer array (TCDPBHS). The TCDPBHS was deployed at depths from 945 to 1270 m throughout the 1999 ruptured slip zone at 1111 m. Three borehole seismometers (BHS1–BHS3) were placed in the hanging wall, and the remaining three (BHS5–BHS7) were placed in the foot wall, with BHS4 near the slip zone. The configuration allowed us to estimate the *Q*-structure of the recent ruptured fault zone. In this study, we estimated *Q* values between BHS1 and BHS4, Qs_1 (Qp_1) at the fault zone and between BHS4 to 2 km in depth, Qs_4 (Qp_4) beneath the fault zone. We utilized two independent methods, the spectral ratio and spectral fitting analyses, for calculating the *Q* value of Qs_1 (Qp_1) in order to provide a reliability check. After analyzing 26 micro-events for *Qs* and 17 micro-events for *Qp*, we obtained consistent *Q* values from the two independent methods. The values of Qs_1 and Qp_1 were 21–22 and 27–35, respectively. The investigation for the value of Qs_4 was close to 45, and Qp_4 was 85. These *Qp* and *Qs* values are quiet consistent with observations obtained for the San Andreas Fault at the corresponding depth. A low Qs_1 value for the recent Chelungpu Fault zone suggests that this fault zone has been highly fractured. *Qs* values within the Chelungpu Fault, similar to those within the San Andreas Fault, suggest that the *Q* structure within the fault zone is sedimentary rock independent. However, the possible existence of fluids, fractures, and cracks dominates the attenuation feature in the fault zone.

1. Introduction

The 1999 Chi-Chi earthquake (Mw 7.6) activated the Chelungpu Fault in the western foothills of central Taiwan, resulting in a 90 km long surface rupture along the north–south trend and a 15 km length E–W-trending branch at the northern termination (Fig. 1a). Along the strike, horizontal and vertical surface displacements both increased from south to north and reached a value of approximately 12 m in the northern portion of the fault. In the past, the geometry of the fault has been investigated using dense reflection surveys (Wang et al., 2004). Both strong motion (Shin and Teng, 2001) and GPS data (Lin et al., 2001; Yu et al., 2001) indicate that the majority of co-seismic movement within the Chi-Chi earthquake occurred at the hanging wall rather than at the footwall, suggesting that the footwall was nearly fixed during the earthquake (Heermance et al., 2003). The data is also consistent with the fact that the hanging wall underwent harsher damage than the footwall. In order to gain more understanding regarding earthquake processes and the long-term evolution of the fault, the Taiwan Chelungpu Fault Drilling Project (TCDP) drilled two holes (A and B) with one branch (C) at Dakeng, Taichung City (Fig. 1a), where the large surface slip was observed. Hole A was drilled to a depth of 2 km, and the 1999 slip zone, at the depth of 1111 m, was identified. Fault zone features and dynamic processes have been well addressed by numerous studies (e.g. Ma et al., 2006; Sone et al., 2007; Song et al., 2007; Tanaka et al., 2006; Yeh et al., 2007). Low resistivity, density, velocity, and high *Vp*/*Vs* and Poisson ratios were also characterized in identified fault zone features (Hung et al., 2009; Wu et al., 2007a).

The quality factor *Q*, that defines the energy decay of the structural features, was revealed to have a significant contrast across the Chelungpu Fault in images of Taiwan 3-D attenuation tomography (Wang et al., 2010). Corresponding to fault geometry with a 30° dip angle, the hanging wall is located within a zone that has a lower *Qp*, lower *Qs*, and higher *Qp*/*Qs* in the image surrounding a depth of 10 km. The contrast may suggest the existence of lithologic heterogeneity between the hanging wall and the footwall. Sanders et al. (1995) summarized the relationship among changes in seismic parameters due to changes in rock properties, and considered that an increase in fractural abundance would result in a decrease in *Qp* and *Qs*, accompanied by an increase in *Qp*/*Qs*. The results suggest that the lower *Qp* and *Qs*, and the higher *Qp*/*Qs* of the hanging wall of the Chelungpu Fault may be related to highly fractured features that resulted from severe shaking during rupture.

* Corresponding author.
E-mail address: rita@eqkc.earth.ncu.edu.tw (Y.-J. Wang).

0040-1951/$ – see front matter © 2011 Elsevier B.V. All rights reserved.
doi:10.1016/j.tecto.2011.12.027

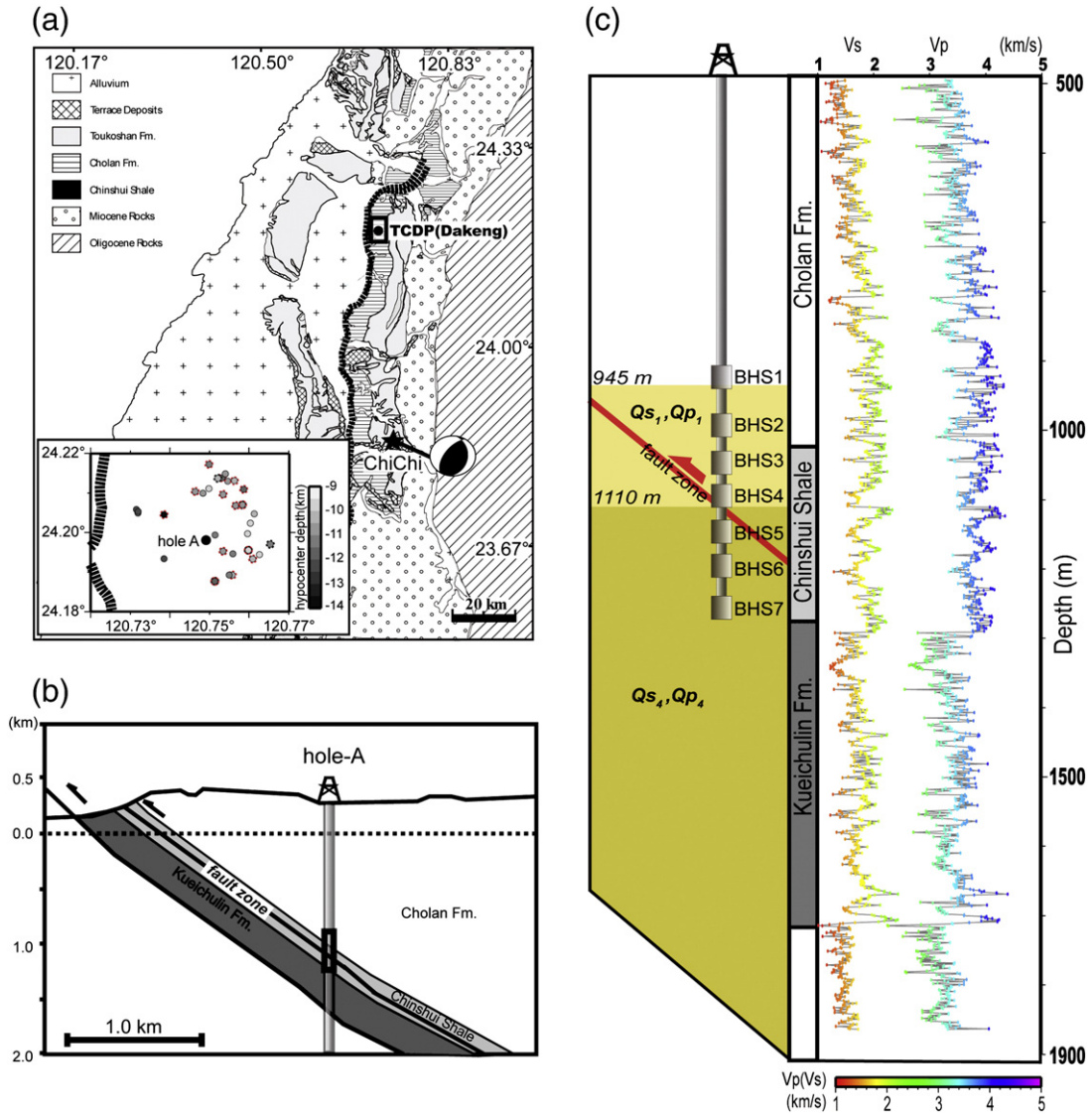

Fig. 1. (a) The geological map of the region near the TCDP drill site (solid dot) (Wu et al., 2007a). The inset shows the distribution of selected micro events in this study. The drill site, Dakeng, is 2.5 km east of the Chelungpu Fault rupture (the wide black dashed line). The location of the Chi-Chi mainshock (asterisk) and its focal mechanism are also shown. The black frame in the lower left inset shows the distribution of the epicenters for thirty-one selected micro events. Events excluded in our data analysis for Qp and Qs with high noise levels are circumscribed in black and red hashed circles, respectively. The color of the circles relative to the events indicates hypocenter depth. (b) A sketch of the geological cross-section near the drill site. Black rectangle marks the location where the TCDPBHS were deployed. (c) The vertical cross-section of hole A showing the depths of 7 deployed TCDPBHS within their corresponding geologic terranes, as displayed in the right-hand bar. The zones in light and dark yellow indicate the extent of depth as defined by Qs_1 (Qp_1) and Qs_4 (Qp_4), respectively. BHS4 is located near the main fault zone (red line).
Referred to Wu et al. (2007a).

However, due to limited resolution in the tomography, the detailed attenuation feature within the fault zone is difficult to determine. Fortunately, after successful TCDP drilling in November 2006, a 7-level vertical borehole seismic array (TCDPBHS) was installed in hole A between the depths of 945 and 1274 m, with intervals of 50–60 m. The array spanned the slip fault zone of the Chelungpu Fault and included the hanging wall and the foot wall (Fig. 1c). Here, using borehole data, we further provide a detailed investigation of Q structure within the fault zone. The primary advantage of using downhole data is avoiding high levels of background noise in order to ensure a higher signal to noise ratio as compared to the surface.

2. A review of the characteristics of the Q value within fault zones

Fault-zone Q is a valuable indicator of the mechanical behavior and the rheology of a fault. In general, the presence of porosity and fluids within a fault zone dramatically reduces Q. Bennington et al. (2008) used three-dimensional tomography in order to characterize the Qp and Qs features of the San Andreas Fault (SAF) in California over 16 km^2. Both Qp and Qs contrasted across the fault were clearly imaged. The high attenuation feature, a Qp and Qs of approximately 50–75 above a 2 km depth on the northeast side of the SAF, was suggested to be attributed to fluid rich rocks. In addition, Blakeslee et al. (1989) analyzed the Qs value of the SAF fault-zone at a depth of 5–6 km using a spectral ratio over the frequency range of 1–40 Hz. By assuming a constant attenuation operator, Blakeslee et al. (1989) estimated a Qs within the fault-zone of 31. Abercrombie (2000) also used the spectral ratio method to calculate the Q in the fault zone, and obtained 50 for Qp and 80 for Qs within 5 km in depth. In addition, Wang et al. (2009a) utilized the quantitative analysis of the correlation coefficients with trapped waves between synthetic and observed waveforms and stated that the shear-wave quality

factor within the Kunlun fault zone was 15 for the upper 1–2 km of depth.

A calculation of the spectral ratio between the two different depth records was the most straightforward way of investigating attenuation on the path in-between. The near-surface low Q surrounding the SAF has also been addressed by many studies in other fault zones. Hauksson et al. (1987) estimated Qp and Qs values using downhole data in the Newport-Inglewood fault zone in the Los Angeles Basin. The authors found that Qp and Qs were 43 and 25, respectively, between 1500 and 420 m in depth, and 108 for Qs from a depth of 420 m to the surface. However, large Qs value observed at 420 m and the surface may be overestimated as a result of the influence of near-surface amplification. The study of Jongmans and Malin (1995), that was located in the Varian Well of the SAF in Parkfield, reported a low Qs of 8 between 298 and 572 m and 65 at a depth of 572–928 m. The average Qs in the top 1 km was 37. In the same location, Abercrombie (2000) also estimated Qp and Qs values of 20 and 10, respectively, at a depth above 300 m. With the increase of Qp and Qs with depth, averaged Qp and Qs values were 33 and 18, respectively, for depths over 1 km. Abercrombie (2000) suggested that the higher estimated Q value of Jongmans and Malin (1995) may have resulted from the longer time-window selected, which included reflected phases and fault zone trapped waves. Abercrombie (1997) also estimated Qs to be 21 ± 7 in the upper 2.9 km, and 47 between 1.5 and 3 km in the Cajon Pass drillhole. By summarizing previous near-surface borehole attenuation results as referenced to various rock types, Abercrombie (1997) further pointed out that these near surface quality factors decreased to very low values, regardless of rock type.

3. Data

The TCDPBHS is a 7-level vertical array that uses a Galperin short period velocity type seismometer. The natural frequency of TCDPBHS is approximately 4.5 Hz. Instruments were installed in July of 2006 and have been operating since November of 2006. A continuous recording system has been successfully monitoring micro earthquake activity surrounding the Chelungpu Fault since that time. From November 2006 to December 2007, the sampling rate was 1000 Hz, and became 200 Hz after 2008. The Galperin angle correction, the orientation correction, and the instrument response removal were carried out prior to the waveform analysis. The TCDPBHS recorded roughly 10 events per day on average for events with a travel time difference in S and P wave arrival times of less than 2 s, and with magnitudes largely less than two. The locations of the events prior to April 2007 were well determined by Lin (2009) using MIMO (Oye and Roth, 2003).

We constrained our event data to those with incidence angles less than approximately 10° using the micro event locations of Lin (2009). As shown in Fig. 1a, in total, 31 micro events with Mw of 0.28 to 1.5 were selected. Five events, that had low signal to noise ratios and that were strongly distorted by the background noise or with visually trapped waves, were excluded. Therefore, a total of 26 events were selected for Qs and 17 events, largely located at depths of 9 to 14 km, were selected for Qp. The vertical projections of these earthquakes were within a horizontal distance of 2 km from the borehole site. The narrow extent allowed us to avoid the influence of lateral lithological variations. Table 1 lists the hypocentral parameters of the micro events utilized in this study.

Although TCDPBHS is a 7-level seismic array, unfortunately, for earthquakes of this size (Mw ~ 0.28–1.5), only BHS1 and BHS4 records had a quality that was suitable for the Q analysis. Fig. 2a and b provides examples of complete observations for the 7 level array for earthquakes of Mw 0.77 and 0.90, respectively. Strong narrow frequency bandwidth noise following the S wave in BHS2 and BHS3 can be clearly seen in Fig. 2a, and also in BHS2, BHS3, and BHS5 in Fig. 2b. The noise recorded, randomly, at BHS2, BHS3, and BHS5 for these micro-earthquakes forced us to not include these data in the spectral analysis. Also unfortunate is that the sensors of BHS6 and BHS7 were not functioning well due to

Table 1
The hypocentral parameters of selected micro events with their relative P and S arrival delays, and the t^* difference between BHS1 and BHS4. The table lists the hypocentral parameters of the micro events selected in this study, as well as the P and S arrival time delays ($t_{p1} - t_{p4}$, $t_{s1} - t_{s4}$), and the t^* difference (Δtp^*, Δts^*) between BHS1 and BHS4. The exact epicenter was located at 120 in longitude and 24 in latitude adding to the value shown. Marker (1) denotes Δtp^* and Δts^* values estimated using the spectral ratio method. Marker (2) displays values assessed using the LSQENP spectral fitting method.

Event no.	Date YY/MM/DD	Time h/s	Mw	Lon. (120+°)	Lat. (24+°)	Depth (km)	Incidence angle (°)	$t_{p1} - t_{p4}$	$t_{s1} - t_{s4}$	$\Delta tp^*(1)$	$\Delta ts^*(1)$	$\Delta tp^*(2)$	$\Delta ts^*(2)$
1	06/11/12	20/1932.60	0.45	0.756	0.213	10.39	9.99	–	0.08	–	−0.0009	–	−0.001
2	06/11/15	17/2976.80	1.51	0.761	0.193	10.02	7.99	–	0.07	–	0.0113	–	0.011
3	06/11/15	18/2784.50	0.50	0.763	0.194	9.87	8.91	0.04	0.06	0.0007	0.0029	0.001	0.003
4	06/11/25	04/657.60	0.52	0.761	0.205	10.36	8.38	0.04	0.05	0.0009	−0.002	0.001	−0.002
5	06/11/25	18/3031.50	0.33	0.755	0.213	10.62	9.33	0.04	0.05	0.0013	0.0008	0.002	0.001
6	06/11/26	16/878.00	0.68	0.765	0.197	11.34	8.88	0.05	–	0.0007	–	0.002	–
7	06/11/26	22/1253.60	0.62	0.759	0.211	11.56	8.54	–	0.05	–	0.0017	–	0.002
8	06/11/29	14/970.45	0.28	0.756	0.195	11.36	4.20	0.04	0.05	0.0006	0.0022	0.001	0.002
9	06/11/30	06/578.90	0.58	0.756	0.189	10.40	6.64	–	0.06	–	−0.0043	–	−0.004
10	07/01/06	21/1262.10	0.84	0.750	0.211	9.98	8.20	0.04	0.08	0.0045	−0.0055	0.004	−0.006
11	07/01/22	11/830.40	0.68	0.755	0.189	11.44	5.77	0.04	0.06	0.0020	−0.0035	0.002	−0.003
12	07/01/23	14/1848.50	0.77	0.760	0.202	9.90	7.63	0.04	0.08	0.0041	0.0036	0.004	0.004
13	07/01/28	21/3432.00	0.77	0.739	0.193	12.41	5.78	0.04	0.05	0.0010	0.0025	0.002	0.002
14	07/01/30	10/2664.30	0.46	0.757	0.207	10.73	6.69	–	0.07	–	−0.0107	–	−0.010
15	07/01/31	17/1520.80	0.40	0.746	0.210	10.87	7.18	–	0.08	–	0.0017	–	0.002
16	07/02/01	10/1153.73	0.47	0.752	0.214	10.17	9.77	0.04	–	0.0013	–	0.001	–
17	07/02/10	19/3154.00	0.49	0.753	0.214	11.57	8.68	–	0.07	–	−0.011	–	−0.009
18	07/02/15	02/2552.55	0.60	0.751	0.199	11.07	1.49	0.04	0.07	0.0026	0.0044	0.001	0.004
19	07/02/25	19/1466.45	1.06	0.748	0.210	10.69	6.92	0.04	0.08	0.0026	−0.0085	0.001	−0.009
20	07/02/27	17/200.60	0.90	0.732	0.205	11.96	9.53	0.04	0.07	0.0021	0.0073	0.002	0.008
21	07/02/27	19/2855.05	0.44	0.731	0.206	12.34	9.57	0.04	0.07	0.0032	0.0054	0.002	0.005
22	07/02/27	19/3083.75	0.44	0.732	0.205	12.35	9.24	0.04	0.07	0.0031	0.0074	0.002	0.008
23	07/02/28	13/3059.60	0.72	0.754	0.215	10.51	10.31	0.04	0.07	0.0015	−0.0089	0.003	−0.009
24	07/03/16	02/353.32	0.56	0.760	0.200	9.62	6.97	0.04	0.08	0.0004	0.0114	0.001	0.012
25	07/03/31	15/1304.80	0.33	0.753	0.210	10.94	7.00	–	0.09	–	−0.0035	–	−0.004
26	07/04/03	04/2550.88	0.61	0.750	0.217	11.22	10.54	–	0.08	–	−0.0073	–	−0.008
27	07/04/15	02/645.30	0.32	0.753	0.195	10.64	3.03	–	0.08	–	0.0035	–	0.004
28	07/04/15	18/1872.20	0.74	0.739	0.204	13.59	5.59	–	0.08	–	0.0035	—	0.003

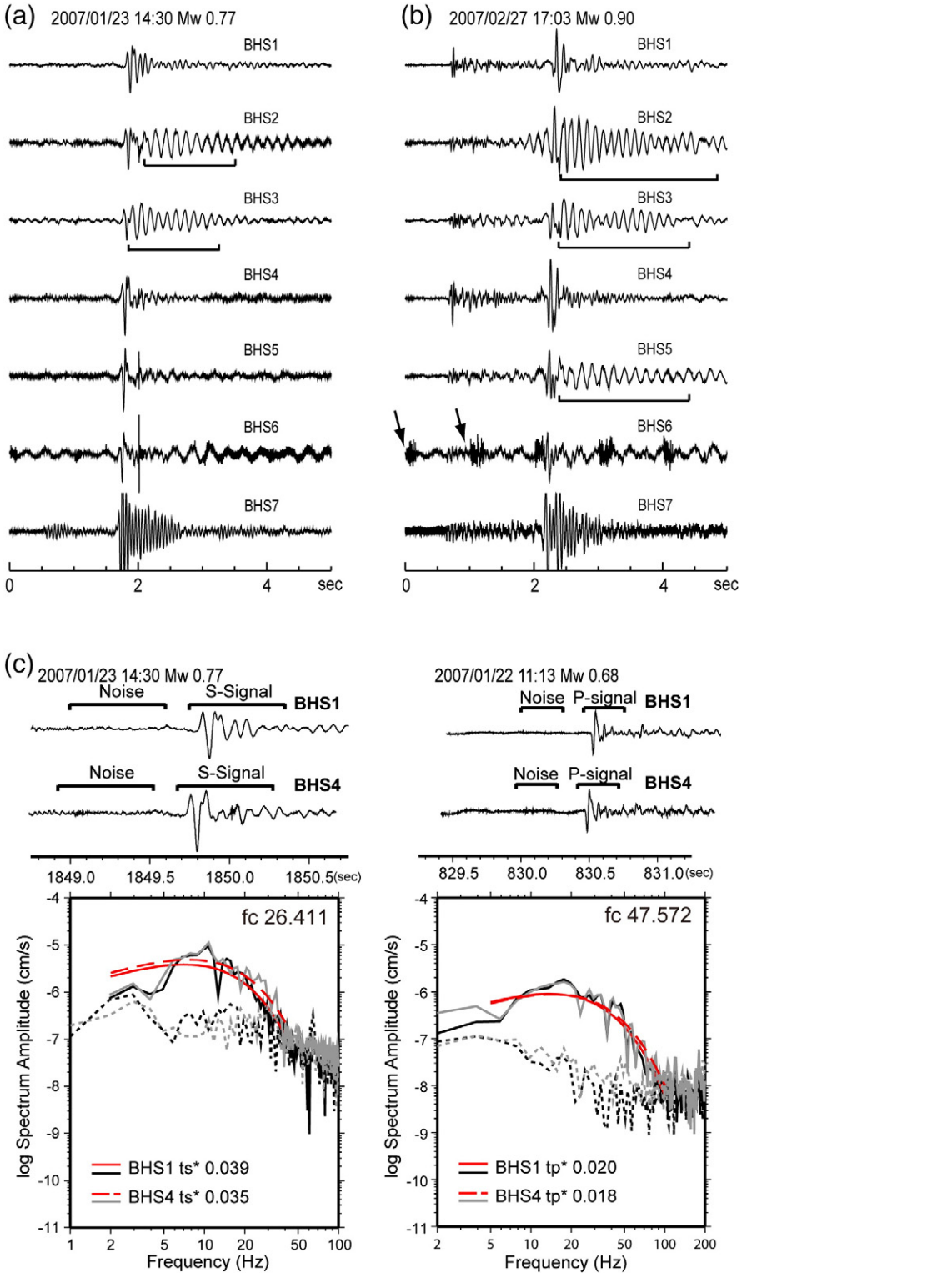

Fig. 2. (a)(b) An example of the complete observations for the TCDPBHS array for events on 23 January 2007 (Mw 0.77) and 27 February 2007 (Mw 0.90), respectively. The waveforms for each event are shown within the same time axis and amplitude scale. Black marks indicate the time-window of strong narrow frequency bandwidth noise that occurred following the *S* wave. The arrows indicate electric noise in the BHS6 records. (c) The *P* (right) and *S* (left) wave signals, and the noise spectra of a specific event that were received at BHS1 and BHS4, as well as their adopted waveform windows, are shown above. (Top) Signal records in two second intervals at BHS1 and BHS4 along with their adopted noise and signal windows (solid caps). After performing a Fourier Transform, the signal (solid line) and noise (dashed line) spectra were achieved (below). The signal and noise spectra of BHS1 and BHS4 are shown in black and gray, respectively. Both recorders presented a distinct high signal to noise ratio in the frequency band of 2–40 Hz in the *S* wave spectra and 5–100 Hz in the *P* wave spectra. The solid, dashed lines in red delineates the estimated signal curves for BHS1 and BHS4 relative to the same corner frequency (*fc*), respectively, within the path attenuation operators (ts^* for the *S* wave, tp^* for the *P* wave) that are indicated in the left-hand corner.

instrument conditions. As shown in Fig. 2b, electric noise appeared every 1 s in BHS6, and as narrow frequency bandwidth wave train in BHS7. In light of data quality, we only considered the BHS1 and BHS4 records for our *Q* studies. Although only two borehole seismometers were available, the locations of the two boreholes were in the hanging wall (BHS1, depth = 945 m) and at the slip zone (BHS4, depth = 1110 m) for the 1999 Chi-Chi earthquake. An analysis of the records from the two borehole seismometers still allowed us to understand the *Q* structure in the recent ruptured fault zone from the hanging wall to the footwall. Since the coring depth for the TCDP went to a depth of 2 km, we separated the analysis of *Q* values into a depth of BHS1 to BHS4 that we named Q_1, a depth of BHS4 to 2 km that we named Q_4, and a depth from 2 km to the depth of the event that we named *Qc*.

The adapted time windows for the *S* wave spectral analysis ranged from 0.4 to 0.8 s. However, 0.4 s is too short of a time interval and would have resulted in an instability in the spectral analysis. Abercrombie (1997) pointed out that a 0.5 s time window difference relative to the primarily 0.5 s window has a very slight influence on the resulting *Q* values. Thus, we chose the time window as a compromise for avoiding contamination by later reflections and for the stability of the spectral calculation for lower frequencies. A mean of a 0.6 s time window for the T component of the *S* wave waveform was considered for the velocity spectral analysis. A 0.3 s time window was utilized for the Z component of the *P* wave performed using the same procedure. Fig. 2c shows examples of *S* and *P* wave waveforms and the spectra recorded by BHS1 and BHS4. The noise spectra selected for the same time window 0.15 s prior to the arrival of the signal are also shown. The distinct feature of the signal above the level of the noise was utilized as the basis for an analysis within the bandwidth from 2 to 40 Hz in the spectra of the *S* wave, and from 5 to 100 Hz for the *P* wave spectra.

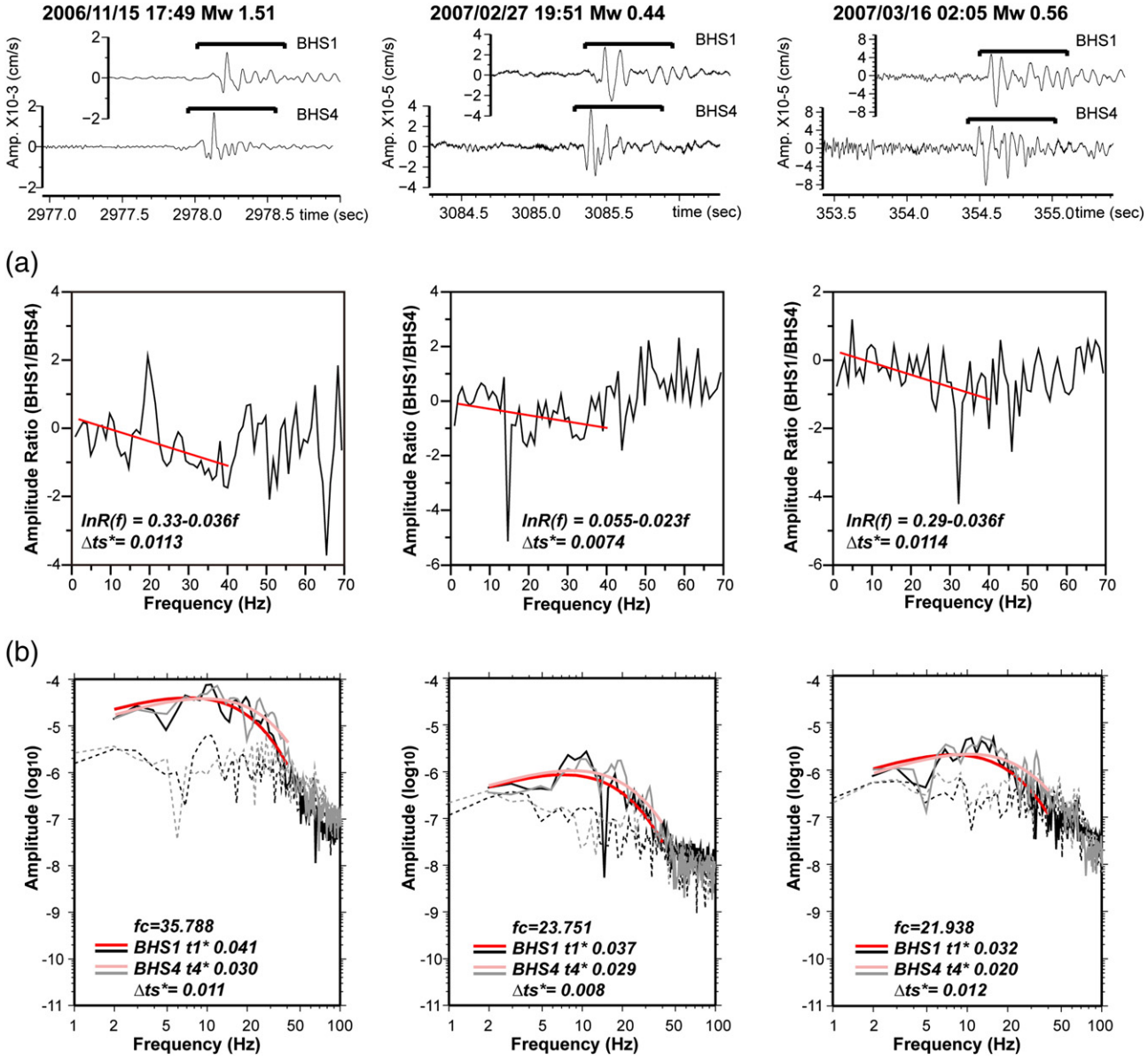

Fig. 3. Examples of the *S* wave spectral analysis using the (a) spectral ratio and (b) spectral fitting of LSQENP for three events. The waveforms recorded at BHS1 and BHS4 with their adopted signal windows (denoted by solid caps) are displayed at the top and are scaled to the same time axis and amplitude level for every specific event. (a) The logarithm plots of the spectral ratio for BHS1 over BHS4 versus frequency. The linear relationship between the spectral ratio and the frequency apparent from 2 to 40 Hz is regressed to the linear trend shown in red. The corresponding regression equation is addressed below with the resulting $t_1^* - t_4^*$ value denoted as Δts^*. (b) The plots of the signal spectra relative to the spectral fitting analysis. The observed signal and noise spectra are depicted with solid and dashed lines (BHS1: black; BHS4: gray), respectively. The optimum fitting curve of the spectra (BHS1: red; BHS4: pink) is estimated from 2 to 40 Hz. Individual t_1^* and t_4^* values were obtained for the same *fc* for every event. Δts^* denotes the difference between t_1^* and t_4^*.

4. Q value determinations

Whether the near surface Q is frequency independent or not remains a controversial issue (Abercrombie, 1997; Aster and Shearer, 1991; Jin et al., 1994; Leary and Abercrombie, 1994). Abercrombie (1997) indicated that the spectral ratios between two different recording depths have a linear slope on a log-linear plot if there is a frequency independent Q. The analysis type has been successfully applied in several studies (Abercrombie, 1997, 2000; Aster and Shearer, 1991; Blakeslee et al., 1989; Hauksson et al., 1987). These studies indicate that shear-wave exponential attenuation models have a linear nature for the log spectral ratio, in general, and appear in the frequency band of 2 to 30 or 40 Hz, suggesting no strong frequency dependence for Q in this frequency band. The spectral ratio analysis of our data, as we discuss later, demonstrates a linear trend for the signal ratio from 2 to 40 Hz in the spectra of the S wave, and 5–100 Hz for the P wave Therefore, a frequency independent Q can also be adopted.

The observed velocity spectrum referring to attenuation can be expressed by the following:

$$A(f) = 2\pi f \Omega_0 \frac{fc^2}{f^2 + fc_2} e^{-\pi f t^*}, \quad (1)$$

where f and fc are the frequency and the corner frequency, respectively; Ω_0 is the long-period plateau value; and t^* is the whole path attenuation operator (e.g., Cormier, 1982; Rietbrock, 2001; Wang et al., 2010). The t^* is related to structural features as the quality factor (Q) and the velocity (V) along the ray-path (S) as follows:

$$t^* = \int_{source}^{receiver} \frac{ds}{QV}. \quad (2)$$

Since the analyses were carried out for BHS1 and BHS4, the $t_1{}^*$ as the whole-path attenuation operator estimated at BHS1 (depth = 945 m) can be described by the following:

$$t_1{}^* = \frac{ds_{k-2}}{Q_c V_c} + \frac{ds_{2-1.11}}{Q_4 V_4} + \frac{ds_{1.11-0.945}}{Q_1 V_1} \quad (3)$$

where $ds_{i\text{-}j}$ denotes the path distance from a depth of i to j km. The Q and V denote the compressional or shear wave quality factor and the corresponding seismic wave velocity within the traveled depth range. The $t_4{}^*$, as the t^* value, observed at BHS4 (depth = 1110 m) can be shown as follows:

$$t_4{}^* = \frac{ds_{k-2}}{Q_c V_c} + \frac{ds_{2-1.11}}{Q_4 V_4}. \quad (4)$$

Thus, the attenuation feature between BHS1 and BHS4 defined as Q_1 refers to the following:

$$t_1{}^* - t_4{}^* = \frac{ds_{1.11-0.945}}{Q_1 V_1} = \frac{t_1 - t_4}{Q_1} \quad (5)$$

and can be calculated directly using the travel time delay of signal arrivals ($t_1 - t_4$) with known $t_1{}^* - t_4{}^*$ values. The time delays between BHS1 and BHS4 for P and S waves of selected events are provided in Table 1, and are approximately 0.04 and 0.07 s, respectively.

The value of $t_1{}^* - t_4{}^*$, as the difference of two path attenuation operators, can be determined by two ways, as follows: 1) using the spectral ratio of the records of BHS1 and BHS4 to directly obtain $t_1{}^* - t_4{}^*$, or 2) using non-linear least-squares (LSQENP) spectral fitting (Wang et al., 2010) based on individual records of BHS1 and BHS4 for corresponding t^* values.

4.1. Spectral ratio analysis

The logarithm of a spectral ratio between a shallow and deeper recording for a specific event can be written as follows:

$$\ln R(f) = \ln(A) - \pi f (t_1{}^* - t_4{}^*) \quad (6)$$

(Abercrombie, 2000). $R(f)$ is the amplitude ratio, and A is the amplification. The same source and instrument response eliminate source and instrument effects. Thus, the slope of the linear-log spectral ratio plot versus the frequency indicates a value of $\pi(t_1{}^* - t_4{}^*)$. Fig. 3a shows three examples of S wave spectral ratio logarithm plots together with their adopted signal windows, as shown above. The linear relationship with frequency is apparent from 2 to 40 Hz. Beyond 40 Hz, the slope of the ratio varies due to distortion of the noise. Hereafter, we use Δts^* and Δtp^* as the $(t_1{}^* - t_4{}^*)$ values of the S and P spectra, respectively. Therefore, the corresponding Δts^* and Δtp^* values we determined are

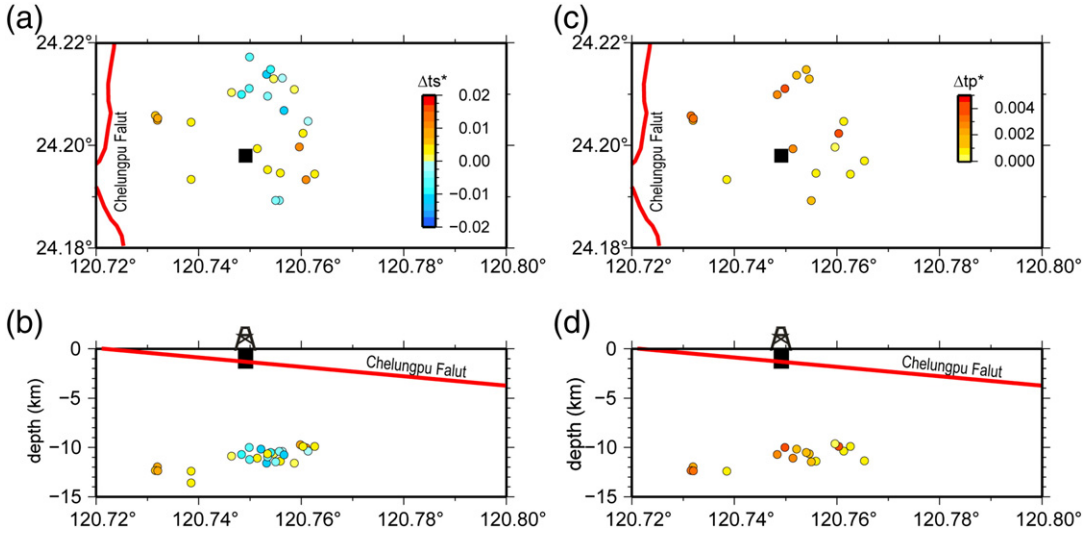

Fig. 4. The distributions of Δts^* and Δtp^* values relative to the epicenter of the events, (a) and (c) map view; (b) and (d) vertical cross sections. (a) and (c) The colors of the circles indicate the Δts^* and the Δtp^* value estimated using the spectral ratio. The Chelungpu Fault is delineated with a red line. The positive t^* difference is expressed with a warm color, and the negative with a cool color. Black squares indicate the location of hole A. (b) and (d) The distributions of Δts^* and Δtp^* are shown with a vertical profile along the east–west direction using the same annotation as displayed in (a) and (c). The length scale of the vertical to the horizontal is approximately 1:5.

listed in Table 1. Fig. 4 shows the distribution of the Δts^* and the Δtp^* values of these events. Generally, the $t_1{}^*$ of BHS1 is expected to be larger than the $t_4{}^*$ of BHS4 for a greater decay in energy due to travel over a longer distance. However, 11 of 26 events with values of $(t_1{}^* - t_4{}^*)$ for *S* waves less than zero were found, and, as shown in Fig. 4a, these events came from the northeastern direction. The phenomenon did not appear for Δtp^* values (Fig. 4c and d). Fig. 5a shows logarithm plots for the three negative Δts^* for these events. They, indeed, display a reverse trend in slope, and the waveforms recorded by BHS1 and BHS4 are quite similar. However, the pulse durations for BHS1 are smaller than those for BHS4, and the amplitude at BHS1 is slightly larger than the one at BHS4, suggesting that the negative Δts^* values for these events did not originate from an error in regression. A possible reason for these negative Δts^* anomalies may be related to a sharp variation in structural properties or to the multi-reflective effect associated with the eastern dip geometry of the Chelungpu Fault. For this work, in order to address *Qs* structure within the fault zone, we only considered 15 events that had positive Δts^* values. The estimated, by considering the *P* and *S* wave travel time delays as listed in Table 1, Qs_1 (the Q_1 value estimated using the *S* wave) and Qp_1 (the Q_1 value estimated using the *P* wave) values are shown with a gray bar in Fig. 6a and b, respectively. The estimated Qs_1 is within the values 6 and 61 and Qp_1 is within 10 to 100. Most values are, however, around 20 in *Qs*. The average Qs_1, and Qp_1 from this analysis is 22 and 35, respectively.

4.2. Spectral fitting of LSQENP

We also estimated the t^* value for every individual record by spectrum fitting the LSQENP algorithm (Marquardt, 1963) derived by Wang et al. (2010). The velocity spectrum analysis utilized two calculation steps of non-linear least squares in order to determine the t^* value. In the first step, Ω_0, *fc*, and t^* were obtained for every individual ray path by minimizing the residuals of the observed and theoretical spectrum. Then, for each individual event, a corner frequency was obtained by averaging the

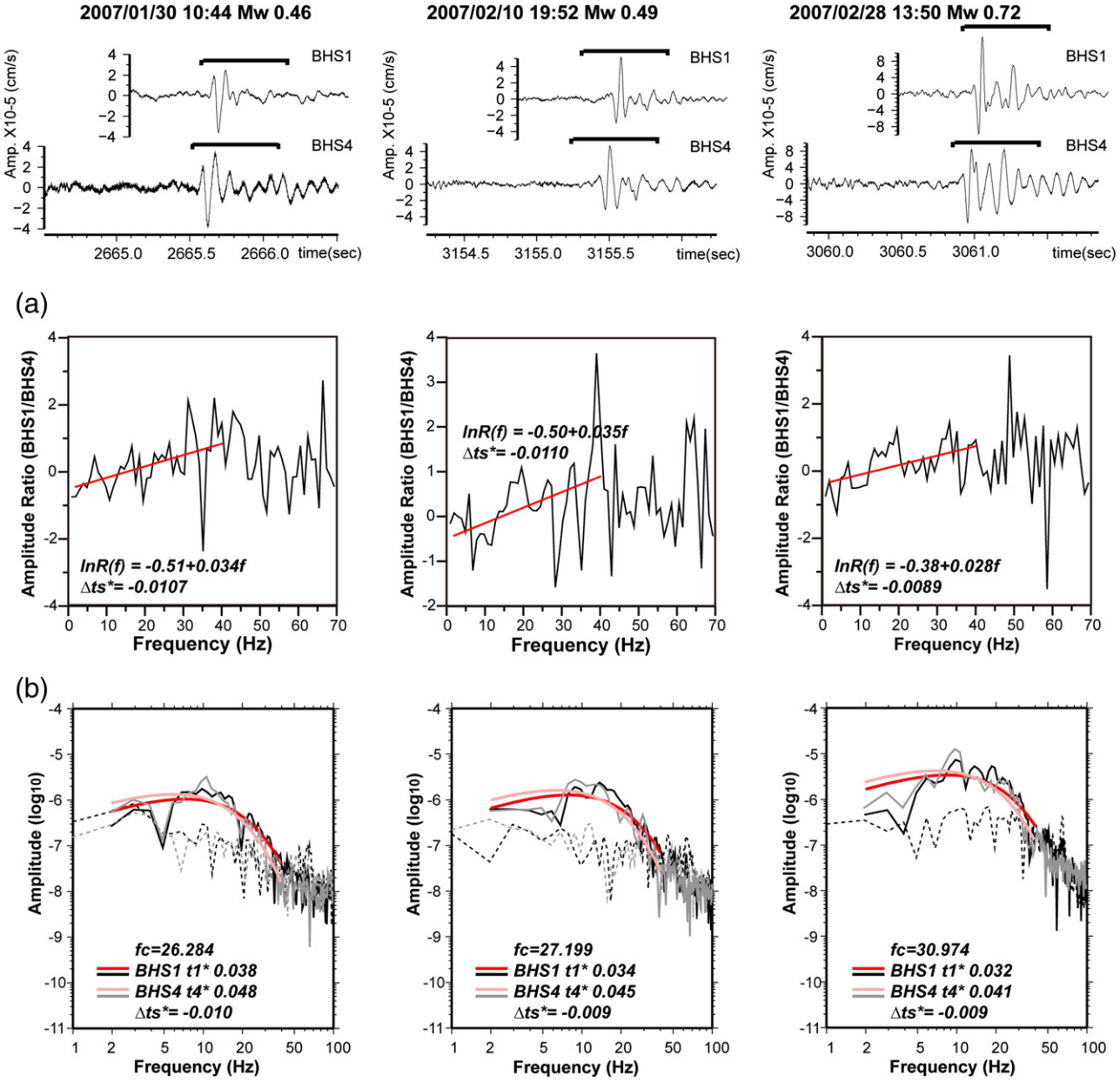

Fig. 5. Examples of the spectral analysis for negative Δts^* anomalies using (a) the spectral ratio and (b) the spectral fitting of LSQENP for three events — 30 January 2007 (Mw 0.46), 10 February 2007 (Mw 0.49), and 28 February 2007 (Mw 0.72). The notations on the figure are the same as in Fig. 3.

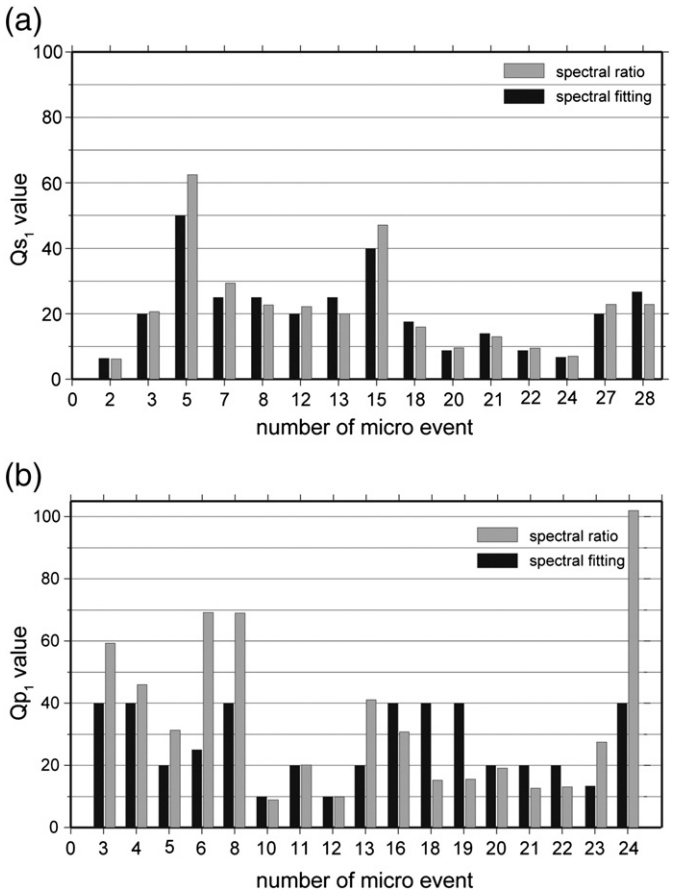

Fig. 6. (a) Qs_1 values relative to 15 micro events. (b) Qp_1 values relative to 17 micro events. Only the values assessed from normal Δts^* are shown in (a). The number of micro event follows the order of events listed in Table 1. Bars in gray and black show the Qs_1 (Qp_1) values estimated using the spectral ratio and spectral fitting, respectively.

values of *fc* recorded by two borehole seismometers for individual events. Therefore, the obtained *fc* was fixed for the second step of the LSQENP spectral fitting for the estimation of the t^* value. Fig. 2c displays one example of *P* and *S* spectral fitting for the adopted time window. We fit the spectra in the frequency band from 2 to 40 Hz for *Qs* and from 5 to 100 Hz for *Qp* that had a high signal to noise ratio. Fig. 3b shows examples of *S* wave spectra fitting following a spectral ratio analysis. The Δts^* values subtracted from individual records of BHS1 and BHS4 were consistent with values estimated using the slope of the spectral ratio analysis. For comparison, the Δts^* values obtained using the spectral ratio method and the spectral fitting method are also listed in Table 1 and Fig. 7, respectively. The values obtained from these two methods are very consistent, even for events with a negative Δts^* for the *S* wave spectra. Estimated Qs_1 values obtained from the positive Δts^* of 15 events, and the Qp_1 value are also shown in Fig. 6. Qs_1 values ranged from 6 to 50 with an average value of 21. The estimated mean Qp_1 value was 27.

Qp_4 and Qs_4 values were estimated using Eq. (4). The *Qc* for *P* and *S* waves were referenced to the *Qp* and *Qs* model of Wang et al. (2010), 240 and 166, respectively. The *Vc* for *P* and *S* waves, obtained using the high resolution velocity model of Wu et al. (2007b), was 2.44 and 4.45 km/s, respectively. The detailed velocity model was measured with logging data at the shallow depth (Wu et al., 2007a). The V_4 was 1.72 km/s for the *S* wave and 3.44 km/s for the *P* wave. Using Eq. (4), we estimated the Qp_4 (the Q_4 value of the *P* wave) and Qs_4 values (the Q_4 value of the *S* wave) as shown in Fig. 8. In general, overall Qs_4 values were larger than Qs_1 values by a factor of two; and, the resulting Qp_4 and Qs_4 were estimated to be 45 and 85, respectively.

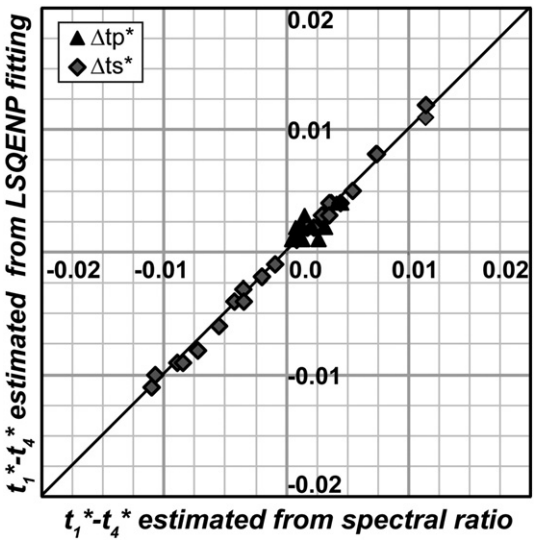

Fig. 7. A comparison of the value of the t^* difference obtained using the spectral ratio and spectral fitting methods. The vertical axis indicates the value estimated by spectral fitting, and the horizontal axis indicates the one estimated using the spectral ratio. The t^* differences estimated by *P* and *S* waves are denoted as triangles and diamonds, respectively. The solid line in black represents the excellent consistency of the values estimated using the two methods.

5. Discussion

The value of Qs_1 represents the attenuation structure on the fault zone between 945 and 1110 m, and is relatively thin in thickness as compared to 10 km depth events. In order to confirm the resolving capability of our methods to this thin layer, we designed a test to assess the *Q* value by simulating waveforms from the Frequency–Wavenumber (FK) synthetic seismogram scheme (Zhu and Rivera, 2002). As shown in Fig. 9a, we constructed a 10 km depth structure with a 0.16 km thickness layer in the depth from 0.95 to 1.11 km. The *S* wave velocities, and the *Qs* values in the thin layer and the deeper depth of 1.11–10 km were $Vs = 1.88$ km/s, and $Qs = 21$; and $Vs = 2.44$ km/s, and $Qs = 166$, respectively.

As shown in Fig. 9a, stations L and H were schematically placed above and below the thin layer. We placed the source at the depth of 10 km. Fig. 9b shows the comparison of synthetic *SH* waveforms and the spectra of stations L and H. Synthetic test indicated that the waveform at station L had a slightly smaller amplitude and a broader waveform due to the influence of the thin low *Qs* zone. As shown in Fig. 9c, the spectral ratio of these two waveforms had a slope of −0.011. The ratio refers to a *Qs* value of approximately 20 from Eq. (6). The value is quite consistent with the original *Qs* of 21 as set in the model. The results of the synthetic test suggest that the method has a suitable resolving capability, regardless of the relatively thin low *Q* layer over the large travel distance.

Following drilling, a suit of comprehensive geological logs were run in order to collect seismic velocities, densities, anisotropy, and borehole images from 500 to 1860 m. Wu et al. (2007a) analyzed fracture densities selected from FMS (Formation Micro Scanner) and FMI (Formation Micro Imager) in 10 m intervals and found that 63% fractures were found between 500 and 1100 m, with nearly 50% of the fractures concentrated between 900 and 1100 m. The number of fractures decreased gradually between 1100 and 1500 m and then rapidly diminished below 1500 m. Velocity logs displayed a gradual increase in *P* and *S* wave velocities due to an increase in the confining pressure with depth. *P* wave velocities ranged from 2.27 km/s at a depth of 551 m, to 5.47 km/s at a depth of 1668 m. The *S* wave velocities increased from 1.4 km/s at a depth of 597 m, to 2.98 km/s at a depth of 1705 m. The overall resistivity of the formations encountered in the TCDP was low, from 20 to 50 Ω-m between depths of 587 and

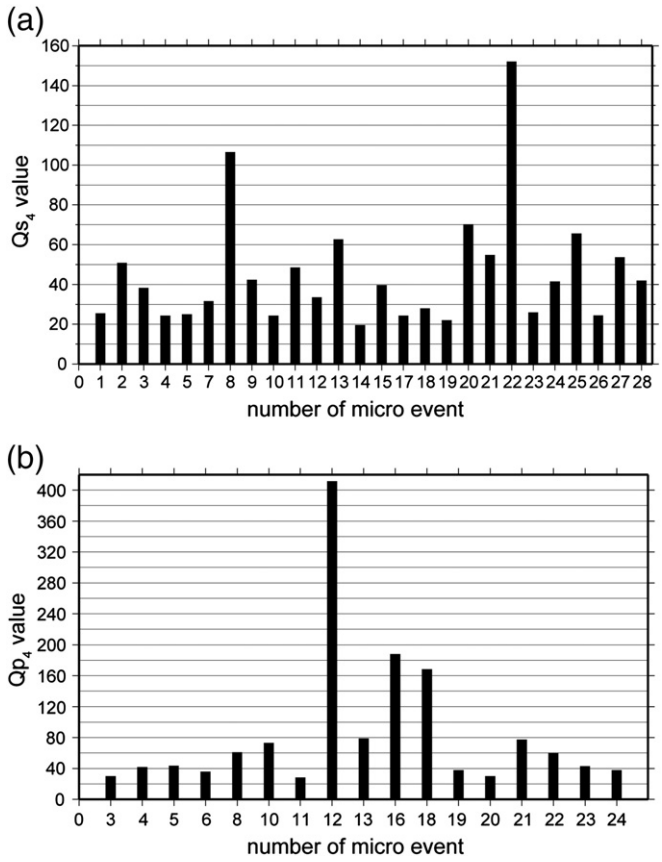

Fig. 8. (a) Qs_4 values relative to 26 micro events that were estimated using a spectral fitting analysis. (b) Qp_4 values relative to 17 micro events that were estimated using a spectral fitting analysis. The number of micro events follows the order of events listed in Table 1.

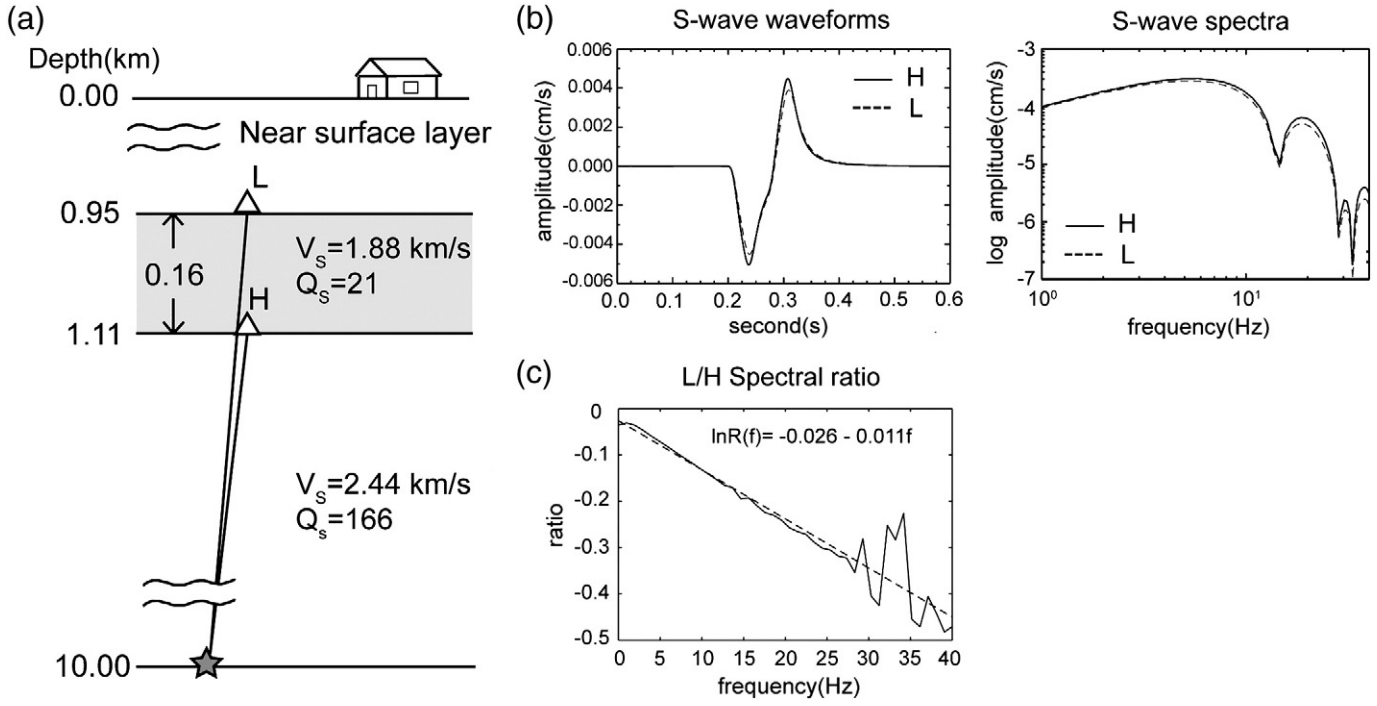

Fig. 9. The model we developed for testing the resolving capability of our method for the thin layer. (a) The simple model we used provides a 2 layer structure from 0.95 to 10.00 km. The source denoted by a star is located at 10 km depth. Two stations, that are represented by triangle symbols, L and H, were located in the top of the low Q thin layer at a depth of 0.95 km, and the top of the host rock layer at the depth of 1.11 km, respectively. (b) Synthetic *SH* waveforms for the H and L stations are shown with solid black and dotted lines, respectively, in the left figure. The corresponding synthetic *SH* spectra for the two stations are shown in the right figure. (c) The spectral ratio of the *SH* wave records for the L and H stations is shown with a solid line. The equation of the regression line (dashed line) for the spectral ratio is addressed above.

1856 m. The authors also found that the most significant changes in *Vp*, *Vs* (Fig. 1c), and resistivity occurred at a depth of 1110 m. Hung et al. (2009) suggested that the *Vp*/*Vs* ratio has an average value of 2.08 (equivalent to a Poisson's ratio of 0.35), but can reach up to 2.4 (Poisson's ratio of 0.4) in highly fractured fault zones. The fault zone (1111 m depth) exhibited the lowest resistivity, and had values that were approximately 40% less than adjacent host rocks. Also, low density, *Vp*, and *Vs* with an approximate 20–25% reduction, but a high *Vp*/*Vs* (~2.4) and Poisson ratio (~0.4) are displayed. In spite of the above observations, no temperature anomaly was observed at the fault zone Hung et al. (2009). The fluid content was also determined to be higher in the main fault zone area as compared to the surrounding rocks (Hung et al. (2009) Yeh et al., 2007). The logging data indicated that the low density, *Vp*, and *Vs*, together with high *Vp*/*Vs* and Poisson ratios at the fault zone could be attributed to the large amount of fractures and fluids. The Qs_1/Qp_1 ratio estimated in this study is 0.6–0.8, which also suggests that the fault zone is located within an area of high fluid content. The velocity ratios of the fault zone to the layer below it for *Vp* and *Vs* are 0.91 and 0.79, respectively. The stronger variation in *Vs* yields to the significant negative Δts^*, rather than Δtp^*. The Chelungpu Fault is an eastern dipping structure, and BHS4 was placed near the fault zone. Most of our data was obtained from the eastern side of the fault. When an incident wave propagates through the main fault zone from a downdip direction, low velocity makes the refracted wave move away from the receiver (BHS4). Alternatively, BHS4, then, possibly receives a multi-reflected wave propagating within the fault zone that decays in energy more than the refracted wave propagating toward BHS1. The interpretation can also be verified using Qs_4 values with negative Δts^* properties that are generally smaller than those with positive Δts^* values. Otherwise, negative Δts^* may also be explained by the sharp variation of lithological properties as fluid content within the area of the fault zone. The *Qs* of partial saturated sandstones was larger than the *Qs* in the fully saturated condition. However, *Qp* displayed contrary behavior (Winkler and Nur, 1982), in which the value of partial saturated sandstones is smaller than the value in the fully saturated sandstones. Thus, the negative values in Δts^* isn't exhibited in Δtp^*.

Additionally, negative Δts^* values may also result from the reflected energy accumulating in BHS1. Wang et al. (2002) ran a series of seismic reflection sections along the north–south profile of the Chelungpu Fault and found that the dip angle of each section varied in an up-and-down manner, leading to an undulating structure for the Chelungpu Fault surface in the north. The drilling site, Dakeng, is located in the concave portion of the undulation. The south dip of the northern plane may also result in a wave being reflected into the BHS1. The extra accumulation of energy could be another factor contributing to negative Δts^* values.

In this study, the Qp_1 and Qs_1 obtained using positive Δts^* data were 21–22 and 27–35, respectively, for a depth of 945 to 1110 m. The Qp_4 and Qs_4 below the slip zone from a depth of 1110 to 2000 m were 45 and 85, respectively. The obtained *Q* values are similar to the *Q* values obtained for the SAF fault zone, as estimated by Abercrombie (2000), Bennington et al. (2008), and Blakeslee et al. (1989). By comparing the *Qs* value to the neighborhood of the main fault zone, a region within 5 km east of the drilling site, the *Qs* value within the top 1 km depth was approximately 80 when using the *Qs* tomography of Wang et al. (2010). A much smaller Qs_1 value at the fault zone is consistent with the common explanation that the fault zone fractures to a greater extent than the surrounding area.

Good agreement for Qs_1 and Qs_4 with *Qs* values estimated near fault zones of California (Abercrombie, 1997, 2000; Hauksson et al., 1987; Malin et al., 1988) at the corresponding depth also suggests less influence for rock types on the reduction of the *Q* value. Based on the work of Yeh et al. (2007), the stratigraphy appears to be the following: Cholan formation for the early Pleistocene to the late Pliocene at depths of 500–1027 m; Chinshui Shale for the early Pliocene at depths of 1027–1268 m; and a Kueichulien formation for the late Miocene to the early Pliocene at depths of 1268–1712 m. The main fault zone in the Chelungpu Fault occurs in Chinshui Shale, which is dominated by claystone with minor amounts of siltstone and muddy sandstone. The claystone beds generally coarsen upward into siltstones with a strongly- to moderately-bioturbated texture, and a few coarsening-upward successions may be capped by up to 5 m of thick muddy sandstone. Overlying Chinshui Shale is the Cholan Formation, with the Kueichulin Formation lying below (Fig. 1b). The dominant lithologies within the Cholan Formation are sandstone, siltstone, and claystone. The formation consists of a series of upward-coarsening successions. Each succession is characterized by claystone at the base that, upward, becomes siltstone and, at the top, very thick sandstone. The Kueichulin Formation is composed of sandstone and bioturbated clayey siltstone. An overall upward increase in clay content and an upward decrease in grain size were found at this formation (Lin et al., 2007). BHS1 and BHS2 are mainly located within the Cholan Formation. BHS3 is located at the transition zone boundary of the Cholan Formation and Chinshui Shale.BHS4 to BHS7 is located within Chinshui Shale (Fig. 1c). Qs_1 was estimated at the strata of the Cholan Formation and Chinshui Shale, and Qs_4 was obtained for the strata of the Chinshui and Kueichulin Formation. A *Qs* value of 25, as obtained by Hauksson et al. (1987), has been estimated for Pleistocene and Pliocene sediments of the Los Angeles basin that includes marine and non-marine sediments and sandstones. The low *Qs* has been suggested to be reflective of the presence of fluids. Otherwise, a *Qs* of 20, as estimated by Abercrombie (2000), has been suggested for the Tertiary sediments of Parkfield. The consistency of *Qs* values between the Chelungpu Fault and San Andreas Fault implies that the existence of fractures and cracks, and also possibly fluids, may dominate the attenuation feature of near surface materials surrounding the fault zone, considering that the rock type remains rather similar within the area.

In the Cajon Pass drillhole arkosic sandstone and conglomerates were found above 500 m. The drillhole is located within a 3500 m thick Mesozoic crystalline basement that includes fractured granite, granodiorite, and gneiss below. The *Qs* is estimated to be 24 ± 6 in the upper 0.7 to 1.5 km and 47 between 1.5 and 3 km (Abercrombie, 1997, 1998). In Oroville, California the Cleveland Hill Fault zone was encountered at a depth of approximately 305 m. Ophiolite rock within the fault zone is saturated and highly fractured. At this site, the *Qs* for the upper 500 m is 9 (Malin et al., 1988). Abercrombie (1998) compared near surface *Q* values investigated in boreholes in a wide range of rock types, and found that low *Q* values extend below 150 m at Anza (Aster and Shearer, 1991) and at Oroville, below 300 m (Malin et al., 1988). In the Cajon Pass borehole, low *Q* values were observed to extend below 1.5 km. The consistency of near surface low *Qs* values between the Chelungpu Fault, the SAF, and the Cleveland Hill Fault for various rocks also seems to confirm that the *Qs* value decreased to a very low value near the surface regardless of rock type, and that the dominant factor resulting in this low *Qs* may result from the existence of fractures and fluids.

6. Conclusions

In this study, we utilized the TCDP borehole seismometer array data in order to estimate the Qs_1 (Qp_1) value, *Qs* (*Qp*) between BHS1 and BHS4 on the fault zone, and the Qs_4 (Qp_4), *Qs* (*Qp*) value from BHS4 to a depth of 2 km beneath the fault zone. Using the assumption of a frequency independent *Q* and ω^2 source model, the spectral ratio and the LSQENP spectral fitting methods were applied in order to assess Qs_1 (Qp_1) and Qs_4 (Qp_4) values. Using the Frequency–Wavenumber simulation, the synthetic result of forward modeling also confirmed the resolving capability of the two methods for estimating the attenuation feature of a thin layer at the fault zone within 10 km from sources. After analyzing micro-events with incidence angles of less than 10°,

consistent results were obtained using two independent methods. By considering the 15 events with positive ($t_1^* - t_4^*$) values, the Qs_1 was estimated to be 21–22, and the Qs_4 was estimated to be 45. For 17 events, the obtained Qp_1 and Qp_4 were 27–37 and 85, respectively.

By comparing near surface *Qs* values of 80 from *Qs* tomography (Wang et al., 2010) within 5 km east of hole A, the Qs_1 at the fault zone was much smaller, consistent with the fact that the fault zone had been highly fractured. The *Q* value within the Chelungpu Fault was similar to values within the San Andreas Fault at a corresponding depth. The consistency of *Qs* values between the Chelungpu Fault and the San Andreas Fault also implies that fractures and cracks, and, also, possibly fluids, may dominate the attenuation feature of near-surface sedimentary rocks surrounding the fault zone, even with the various sub-groups of materials within the area. The similar low *Qs* value within the investigated Chelungpu Fault to those observed in the San Andreas Fault and the Cleveland Hill Fault suggests that the fractures, cracks, and fluids might be the main mechanism responsible for the *Qs* decreasing, regardless of rock types.

Acknowledgments

We thank the TCDP team, who helped with the deployment of borehole seismometers, following successful drilling at the Chelungpu Fault. Comments and suggestions from the Associate Editor and two anonymous reviewers helped us greatly improve the manuscript. Our work was supported by NSC grant NSC 99-2116-M-008-041, and by CWB MOTC-CWB-99-E-10.

References

Abercrombie, R.E., 1997. Near-surface attenuation and site effects from comparison of surface and deep borehole recordings. Bulletin. Seismological Society of America 87, 731–744.

Abercrombie, R.E., 1998. A summary of attenuation measurements from borehole recordings of earthquakes: the 10 Hz transition problem. Pure and Applied Geophysics 153 (2), 475–487.

Abercrombie, R.E., 2000. Crustal attenuation and site effects at Parkfield, California. Journal of Geophysical Research 105, 6277–6286.

Aster, R.C., Shearer, P.M., 1991. High-frequency borehole seismograms recorded in the San Jcinto Fault zone, Southern California Part 2. Attenuation and site effects. Bulletin. Seismological Society of America 81, 1081–1100.

Bennington, N., Thurber, C., Roecker, S., 2008. Three-dimensional seismic attenuation structure around the SAFOD site, Parkfield, California. Bulletin. Seismological Society of America 98, 2934–2947.

Blakeslee, S., Malin, P., Alvarez, M., 1989. Fault zone attenuation of high frequency seismic waves. Geophysical Research Letters 16, 1321–1324.

Cormier, V.F., 1982. The effect of attenuation on seismic body waves. Bulletin. Seismological Society of America 72, 169–200.

Hauksson, E., Teng, T.A.L., Henyey, T.L., 1987. Results from a 1500 m deep, three-level downhole seismometer array: site response, low Q values, and f_{max}. Bulletin. Seismological Society of America 77, 1883–1904.

Heermance, R., Shipton, Z.K., Evans, J.P., 2003. Fault structure control on fault slip and ground motion during the 1999 rupture of the Chelungpu Fault, Taiwan. Bulletin. Seismological Society of America 93, 1034–1050.

Hung, J.H., Ma, K.F., Wang, C.Y., Ito, H., Lin, W., Yeh, E.C., 2009. Subsurface structure, physical properties, fault-zone characteristics and stress state in scientific drill holes of Taiwan Chelungpu Fault Drilling Project. Tectonophysics 466, 307–321.

Jin, A., Mayeda, K., Adams, D., Aki, K., 1994. Separation of intrinsic and scattering attenuation in southern California using TERRAscope data. Journal of Geophysical Research 99, 17835–17848.

Jongmans, D., Malin, P.E., 1995. Microearthquake S-wave observations from 0 to 1 km in the Varian well at Parkfield, California. Bulletin. Seismological Society of America 85, 1805–1820.

Leary, P., Abercrombie, R., 1994. Frequency dependent crustal scattering and absorption at 5–160 Hz from coda decay observed at 2.5 km depth. Geophysical Research Letters 21, 971–974.

Lin, Y.Y., 2009. Observation and Scaling of Microevents from TCDP Borehole Seismometers. MS thesis, Department of Geophysics, National Central University, pp. 131.

Lin, A., Ouchi, T., Chen, A., Maruyama, T., 2001. Co-seismic displacements, folding and shortening structures along the Chelungpu surface rupture zone occurred during the 1999 Chi-Chi (Taiwan) earthquake. Tectonophysics 330 (3–4), 225–244.

Lin, A.T., Wang, S.M., Hung, J.H., Wu, M.S., Liu, C.S., 2007. Lithostratigraphy of the Taiwan Chelungpu-fault Drilling Project-A borehole and its neighboring region, central Taiwan. Terrestrial Atmospheric and Oceanic Sciences 18 (2), 223–241.

Ma, K.F., Tanaka, H., Song, S.R., Wang, C.Y., Hung, J.H., Tsai, Y.B., Mori, J., Song, Y.F., Yeh, E.C., Soh, W., Sone, H., Kuo, L.W., Wu, H.Y., 2006. Slip zone and energetics of a large earthquake from the Taiwan Chelungpu-fault Drilling Project. Nature 444 doi:10.1038.

Malin, P.E., Waller, J.A., Borcherdt, R.D., Cranswick, E., Jensen, E.G., Van Schaack, J., 1988. Vertical seismic profiling of Oroville microearthquakes: velocity spectra and particle motion as a function of depth. Bulletin of the Seismological Society of America 78 (2), 401–420.

Marquardt, D.W., 1963. An algorithm for least-squares estimation of nonlinear parameters. Journal of the Society for Industrial and Applied Mathematics 11, 431–441.

Oye, V., Roth, M., 2003. Automated seismic event location for hydrocarbon reservoirs. Computers and Geosciences 29, 851–863.

Rietbrock, A., 2001. P wave attenuation structure in the fault area of the 1995 Kobe earthquake. Journal of Geophysical Research 106 (B3), 4141–4154.

Sanders, C.O., Ponko, S.C., Nixon, L.D., Schwartz, E.A., 1995. Seismological evidence for magmatic and hydrothermal structure in Long Valley caldera from local earthquake attenuation and velocity tomography. Journal of Geophysical Research 100 (B5), 8311–8326.

Shin, T.C., Teng, T., 2001. An overview of the 1999 Chi-Chi, Taiwan, earthquake. Bulletin of the Seismological Society of America 91, 895–913.

Sone, H., Yeh, E.C., Nakaya, T., Hung, J.H., Ma, K.F., Wang, C.Y., Song, S.R., Shimamoto, T., 2007. Mesoscopic structural observations of cores from the Chelungpu fault system, Taiwan Chelungpu fault drilling project Hole A, Taiwan. Terrestrial Atmospheric and Oceanic Sciences 18, 359–377.

Song, S.R., Kuo, L.W., Yeh, E.C., Wang, C.Y., Hung, J.H., Ma, K.F., 2007. Characteristics of the lithology, fault-related rocks and fault zone structures in TCDP hole-A. Terrestrial Atmospheric and Oceanic Sciences 18, 243–269.

Tanaka, H., Chen, W.M., Wang, C.Y., Ma, K.F., Urata, N., Mori, J., Ando, M., 2006. Frictional heat from faulting of the 1999 Chi-Chi, Taiwan earthquake. Geophysical Research Letters 33, 16316. doi:10.1029/2006GL026673.

Wang, C.Y., Li, C.L., Su, F.C., Leu, M.T., Wu, M.S., Lai, S.H., Chern, C.C., 2002. Structural mapping of the 1999 Chi-Chi Earthquake Fault, Taiwan by seismic reflection methods. Terrestrial Atmospheric and Oceanic Sciences 3, 211–226.

Wang, C.Y., Li, C.L., Lee, H.C., 2004. Constructing subsurface structures of the Chelungpu Fault to investigate mechanisms leading to abnormally large ruptures during the 1999 Chi-Chi earthquake, Taiwan. Geophysical Research Letters 31, L02608. doi:10.1029/2003GL018323.

Wang, C.Y., Mooney, W.D., Ding, Z., Yang, J., Yao, Z., Lou, H., 2009a. Shallow seismic structure of Kunlun fault zone in northern Tibetan Plateau, China: implications for the 2001 Ms8. 1 Kunlun earthquake. Geophysical Journal International 177, 978–1000.

Wang, Y.J., Ma, K.F., Mouthereau, F., Eberhart-Phillips, D., 2010. Three-dimensional Qp- and Qs-tomography beneath Taiwan orogenic belt: implications for tectonic and thermal structure. Geophysical Journal International 180, 891–910.

Winkler, K.W., Nur, A., 1982. Seismic attenuation: effects of pore fluids and frictional-sliding. Geophysics 47 (1), 1–15.

Wu, H.Y., Ma, K.F., Zoback, M., Boness, N., Ito, H., Hung, J.H., Hickman, S., 2007a. Stress orientations of Taiwan Chelungpu-Fault Drilling Project (TCDP) hole-A as observed from geophysical logs. Geophysical Research Letters 34, L01303. doi:10.1029/2006GL028050.

Wu, Y.M., Chang, C.H., Zhao, Li, Shyu, J.B.H., Chen, Y.G., Sieh, K., Avouac, J.P., 2007b. Seismic tomography of Taiwan: improved constraints from a dense network of strong motion stations. Journal of Geophysical Research 112, B08312. doi:10.1029/2007JB004983.

Yeh, E.C., Sone, H., Nakaya, T., Ian, K.H., Song, S.R., Hung, J.H., Lin, W., Hirono, T., Wang, C.Y., Ma, K.F., Soh, W., Kinoshita, M., 2007. Core description and characteristics of fault zones from Hole-A of the Taiwan Chelungpu-fault Drilling Project. Terrestrial Atmospheric and Oceanic Sciences 18 (2), 327–357.

Yu, S.B., Kuo, L.C., Hsu, Y.J., Su, H.H., Liu, C.C., Hou, C.S., Lee, J.F., Lai, T.C., Liu, C.C., Liu, C.L., Tseng, T.F., Tsai, C.S., Shin, T.C., 2001. Preseismic deformation and coseismic displacements associated with the 1999 Chi-Chi, Taiwan, earthquake. Bulletin of the Seismological Society of America 91 (5), 995–1012.

Zhu, L., Rivera, L.A., 2002. A note on the dynamic and static displacements from a point source in multi-layered media. Geophysical Journal International 148, 619–627. doi:10.1046/j.1365-246X.2002.01610.x.